

Walled Carotid Bifurcation Phantoms for Imaging Investigations of Vessel Wall Motion and Blood Flow Dynamics

Adrian J. Y. Chee, *Graduate Student Member, IEEE*, Chung Kit Ho, Billy Y. S. Yiu, *Member, IEEE*, and Alfred C. H. Yu, *Senior Member, IEEE*

Abstract—As a major application domain of vascular ultrasound, the carotid artery has long been the subject of anthropomorphic phantom design. It is nevertheless not trivial to develop walled carotid phantoms that are compatible for use in integrative imaging of carotid wall motion and flow dynamics. In this paper, we present a novel phantom design protocol that can enable efficient fabrication of walled carotid bifurcation phantoms with: 1) high acoustic compatibility; 2) artery-like vessel elasticity; and 3) stenotic narrowing feature. Our protocol first involved direct fabrication of the vessel core and an outer mold using computer-aided design tools and 3-D printing technology; these built parts were then used to construct an elastic vessel tube through investment casting of a polyvinyl alcohol containing mixture, and an agar-gelatin tissue mimicking slab was formed around the vessel tube. For demonstration, we applied our protocol to develop a set of healthy and stenosed (25%, 50%, and 75%) carotid bifurcation phantoms. Plane wave imaging experiments were performed on these phantoms using an ultrasound scanner with channel-level configurability. Results show that the wall motion dynamics of our phantoms agreed with pulse wave propagation in an elastic vessel (pulse wave velocity of 4.67 ± 0.71 m/s measured at the common carotid artery), and their flow dynamics matched the expected ones in healthy and stenosed bifurcation (recirculation and flow jet formation observed). Integrative imaging of vessel wall motion and blood flow dynamics in our phantoms was also demonstrated, from which we observed fluid-structure interaction differences between healthy and diseased bifurcation phantoms. These findings show that the walled bifurcation phantoms developed with our new protocol are useful in vascular imaging studies that individually or jointly assess wall motion and flow dynamics.

Index Terms—Blood flow dynamics, carotid bifurcation phantom, integrative imaging, vessel wall motion.

I. INTRODUCTION

IT IS well established that various dynamic events arise in human arteries on a cyclic basis [1]. Vessel wall pulsation

Manuscript received February 19, 2016; accepted July 11, 2016. Date of publication July 18, 2016; date of current version November 1, 2016. This work was supported in part by the Natural Sciences and Engineering Council of Canada (RGPIN-2016-04042), the Hong Kong Innovation and Technology Fund (GHP/025/13SZ), and the Research Grants Council of Hong Kong (GRF 785113M).

A. J. Y. Chee, C. K. Ho, and B. Y. S. Yiu are with the Department of Electrical and Electronic Engineering, University of Hong Kong, Hong Kong (e-mail: adrian.chee@hku.hk; kit.ck-ho@hku.hk; billy.yiu@hku.hk).

A. C. H. Yu is with the Department of Electrical and Computer Engineering, University of Waterloo, Waterloo, ON N2L 3G1, Canada (e-mail: alfred.yu@uwaterloo.ca).

Digital Object Identifier 10.1109/TUFFC.2016.2591946

and blood flow are two particular dynamic events that are of clinical interest, and changes in their spatiotemporal dynamics are known to be associated with vascular pathologies such as atherosclerosis [2]–[4]. Accordingly, attempts have been made to noninvasively image and quantify the dynamics of arterial structure and blood flow using ultrasound [5], [6]. While some methods have individually examined arterial wall mechanics [7], [8] and blood flow dynamics [9], [10] (using high frame rate imaging principles), others have sought to simultaneously image arterial wall motion and blood flow [11]–[13]. These latter efforts can potentially give new information on the fluid-structure interactions inside the vasculature and, in turn, provide new insights for vascular diagnostics [14].

To support the development of new ultrasound imaging techniques for gauging the dynamics of arterial wall and blood flow, it is essential to devise phantom test-beds whose vessel wall mechanics and flow dynamics are already known and characterized. These phantoms serve to provide means of calibrating and refining new vascular imaging algorithms prior to applying them for use *in vivo* [15]. One way of creating such a test-bed is to extract arterial specimens from cadavers [16], [17] or animals [18], although the resulting vascular conditions often lack generality because the vascular anatomy cannot be manipulated and its tissue properties tended to deviate from conditions *in vivo*. In contrast, computational phantoms may be devised using analytical equations, finite-element analysis tools, and ultrasound physics simulators [19]–[22]. However, this type of test-bed, even with diligent specification of computational boundary conditions, inherently cannot be adopted to test and troubleshoot hardware-level implementations of new vascular imaging methods. As an alternate solution, vascular phantoms can be constructed *in vitro* using materials that mimic vascular tissue [15]. One commonly used phantom is the straight tube model with elastic wall properties [23]. Yet, the vascular conditions derived from this model are not anatomically realistic because the human vasculature is typically tortuous, especially at branching points where pathological conditions such as atherosclerosis are prone to develop [24].

While the ultrasound community is not short of efforts to devise anatomically realistic phantoms for vascular imaging research, none of the existing fabrication protocols are intended for the testing of new imaging techniques that

simultaneous render arterial wall motion and flow dynamics. For instance, wall-less phantoms of the carotid [25], [26] and renal arteries [27] have been reported, but their inherent lack of vessel wall has limited their application to Doppler ultrasound [28], [29] and flow imaging studies [30]. Design of walled anthropomorphic phantoms has also been attempted using silicone [31] or compliant photopolymers [32], and they have been used to examine the hemodynamics of diseased vasculature [33]–[35] and to test novel contrast imaging modes [36]. However, the elastic properties of silicone and photopolymers cannot be readily tuned, and their acoustic compatibility is at best mediocre. To construct anatomically realistic phantoms with artery-like vessel elasticity and high acoustic compatibility, polyvinyl alcohol (PVA) cryogel may possibly be used as the vessel wall material [37]. In approaching this task, the prior art generally adopted a double lost core strategy that involved the use of low melting point alloys and multiple rounds of investment casting through silicone molding [38], [39]. As such, skilled craftsmanship is inevitably required. This makes it technically cumbersome, if not impossible, to pursue mass production of a repertoire of phantoms with different extents of pathological features to foster evaluation of new vascular imaging methods.

In this paper, we present a new vascular phantom design framework that can efficiently fabricate walled carotid bifurcation phantoms with: 1) vessel elasticity similar to that of human arteries (110–190 kPa [40]), as realized using a PVA-containing mixture for wall construction; 2) varying levels of arterial stenosis; and 3) physiologically relevant flow profiles. We formulated our new framework with the intention of establishing a library of walled carotid phantoms with serial progression of stenosis features, so as to facilitate longitudinal investigations on the performance of imaging techniques that integratively track arterial wall motion and blood flow dynamics. The practical applicability of our new phantoms is demonstrated in this paper through an initial series of experiments involving the plane wave imaging paradigm [41].

Note that our work has been guided by two propositions. First, we posit that, with the impending pervasiveness of 3-D printing technology and computer-aided design (CAD) tools [42], the molds and tools needed for building anatomically realistic vascular phantoms with disease morphologies can be readily created without advanced craftsmanship prerequisites. Second, we surmise that, rather than relying on the previously used double lost core approach to construct vessel tubes [31], [38], [39], a single-stage casting process can be formulated with the help of 3-D printing solutions to streamline the vessel fabrication efficiency. Taken together, these propositions have enabled us to pursue methodological innovations in walled anthropomorphic phantom design that are distinguished from previous efforts on this topic.

II. PHANTOM FABRICATION PROTOCOL

Our new phantom design framework essentially involved four major stages. First, a vessel core was designed using CAD tools, and it was fabricated using 3-D printing technology. Second, using the same tools (CAD drafting and 3-D printing),

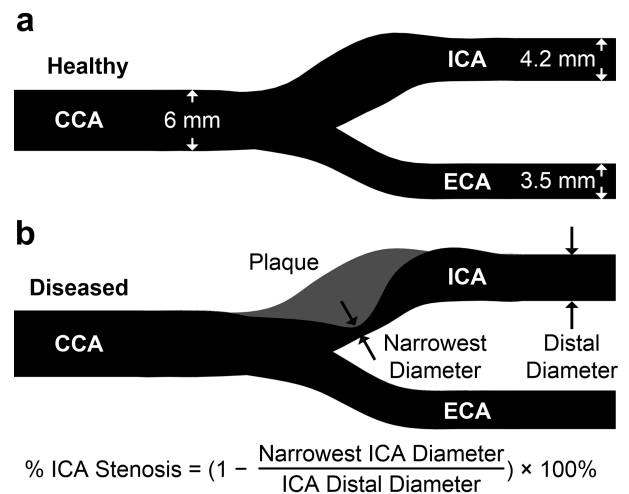


Fig. 1. Overview of the carotid bifurcation geometry used in the new phantom protocol. (a) Three branches are aligned in coplanar orientation: CCA, ICA, and ECA. Dimensions are as labeled. (b) For the diseased geometries, an eccentric plaque is placed at the ICA inlet. Stenosis level is quantified in percentage scale based on the ratio between the narrowest and distal diameters (NASCET criteria).

an outer mold was created based on expanded dimensions of the vessel core. Third, the elastic vessel tube was fabricated by injecting PVA-based vessel wall mixture to fill the cavity between the vessel core and the outer mode, after which the PVA-filled mold was subjected to three freeze-thaw cycles. Once an elastic vessel wall was formed around the vessel core, the phantom was withdrawn from the mold, and its inner core was removed by gently snapping the vessel core to break its mechanical structure for retrieval, thereby forming a luminal void. In the last stage, the vessel tube was mounted onto a phantom box, and an agar-gelatin tissue mimicking slab was cast around the vessel tube. The completed phantom was then connected to a flow pump for operation.

In this work, we have applied our fabrication protocol to construct carotid bifurcation phantoms whose vascular geometry is the same as the one employed in our previous work [32]. Briefly, as illustrated in Fig. 1(a), the bifurcation geometry consists of three branches: common carotid artery (CCA) with 6-mm diameter, internal carotid artery (ICA) with 4.2-mm diameter, and external carotid artery (ECA) with 3.5-mm diameter. It takes on a coplanar structure that is based upon a tuning fork model [43], and the vessel branch parameters are defined such that they are in line with the mean carotid artery diameter of adults [44]. As characterized previously by others [33], [34], the dominant flow patterns of this coplanar bifurcation geometry appear along the central long-axis plane, thus making this geometry suitable for the testing of 2-D vascular imaging methods.

To demonstrate the feasibility of using our new framework to develop a set of phantoms with serial progression of arterial stenosis feature, we have included an eccentric constriction at the entrance to the ICA branch of the bifurcation geometry. The extent of this narrowing, as depicted in Fig. 1(b), is defined on a percentage basis according to the North America Symptomatic Carotid Endarterectomy Trial (NASCET)

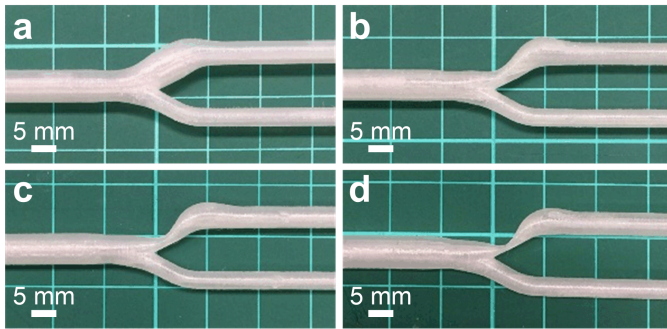


Fig. 2. Photographs of carotid bifurcation vessel cores fabricated using the new phantom protocol's FDM system. (a) Healthy geometry. (b)–(d) Diseased geometries with 25%, 50%, and 75% eccentric stenosis at the ICA inlet.

criteria that were established previously [45]. As a proof of concept, diseased bifurcation phantoms with three stenosis levels (25%, 50%, and 75%) have been made in addition to the healthy bifurcation phantom. Various stages of the fabrication protocol are described in the following sections.

A. Vessel Core Design for Replication of Bifurcation Lumen

1) *Core Model Drafting*: Our phantom design framework first involved creating a CAD model for the vessel core whose geometry is essentially a replicate of the carotid bifurcation lumen. This task was carried out using SolidWorks (Dassault Systemes, Waltham, MA, USA). Note that the three carotid artery branches of our model were equally extended so that the vessel core had a total segment length of 220 mm. For the bifurcation geometries with eccentric stenosis at the ICA inlet, the constriction was realized by shifting the luminal centerline toward the inner wall of the ICA inlet proportionately in accordance with the NASCET criteria [45].

2) *Physical Fabrication Using 3-D Printing*: After drafting the CAD model of the vessel core, it was exported as a stereolithography (STL) file that describes the surface geometry of the drafted model. The STL file was then converted into machine instructions for 3-D printing using an open-source fused deposition modeling (FDM) system (model DX; Creatbot 3D Printer, Zhengzhou, China). Fig. 2 shows the fabricated vessel cores for carotid bifurcation models with healthy and diseased geometries (25%, 50%, and 75% stenosis). Note that, for this 3-D printing operation, a layer thickness of 0.1 mm and a skin thickness of 0.5 mm were adopted, restricting the smallest feature size to 1 mm in diameter. Also, polylactic acid (PLA) thermoplastic was used as the 3-D printing material in view of its rigid but brittle mechanical property that favors vessel core removal in subsequent steps of phantom development. To reduce the structural rigidity of the fabricated vessel core, the FDM operation was carried out with an infill density of 12.5% to create a partial interior void.

B. Outer Mold Design for Construction of Walled Phantom

1) *Mold Model Drafting*: Aside from the vessel core, an outer mold CAD model was also drafted using SolidWorks

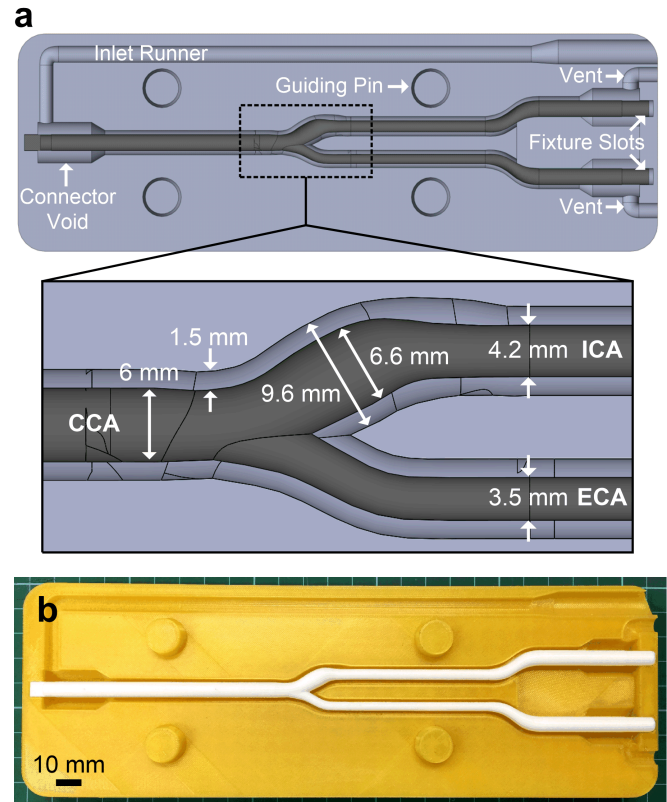


Fig. 3. Illustration of outer mold design in the new phantom protocol. (a) CAD model with key design features annotated. An enlarged view of the dimensions in the bifurcation region is shown. Radial dimensions of the bifurcation void were enlarged by 1.5 mm with respect to the vessel core diameters. (b) Photograph of one fabricated outer mold half (yellow) with the vessel core (white) mounted onto the fixture slot.

to facilitate walled phantom construction. With a dimension of $240 \times 80 \times 25 \text{ mm}^3$, this mold was designed as a solid cuboid with a luminal void that resembled the bifurcation geometry as realized through SolidWorks' Boolean subtraction function. As shown in Fig. 3(a), its luminal dimensions were radially enlarged by 1.5 mm with respect to the vessel core, so as to create a void for vessel wall formation in the next step of phantom development. At the CCA inlet and the two outlets (ECA and ICA) of the enlarged bifurcation void, the luminal dimensions were reduced to that of the vessel core such that fixture slots were naturally created at three carotid branch ends to allow for suspended mounting of the vessel core on the central axis of the enlarged bifurcation void. Also, void replicas of flow connectors were added to the three branch ends so that the fabricated vessel tube can be conveniently plugged into the flow circuit.

2) *Additional Design Features*: A few other technical features were included in our outer mold as illustrated in Fig. 3(a). First, an inlet runner duct and two outlet vents were added to the mold to facilitate unidirectional filling of the vessel wall void with vessel mimicking mixture (and, in turn, avoid trapping air within the wall cavity). Second, to facilitate retrieval of the casted vessel tube, the mold was split into two halves with the split plane aligned to the central long-axis plane of the bifurcation geometry. Third, guiding pins were

added to one side of the halved mold, while their negative replicas were placed in the other half, thereby creating an interlocking mechanism to ensure that the two mold halves were aligned during the vessel wall casting process.

3) *3-D Printing for Direct Use in Vessel Wall Casting*: A physical build of two outer mold halves was created using the same 3-D printing procedure described for vessel core fabrication. The only exception is that an infill density of 25% was used (instead of 12.5% for vessel core production). Doing so effectively enhanced the mechanical strength of the two mold halves such that they would not be prone to breakage. Note that a different PLA color was used for outer mold fabrication to visually discern between the mold and the vessel core [see Fig. 3(b)].

C. PVA-Based Vessel Tube Construction

1) *Vessel Wall Material Formulation*: In preparation for vessel tube construction, a vessel mimicking mixture was formed using an in-house formula. The mixture was consisted of (by weight): 1) 86.7% distilled water; 2) 10% PVA powder (341584; Sigma-Aldrich, St. Louis, MO, USA), as required to form elastic vessel walls (through polymeric crosslinking); 3) 3% graphite with particle diameter less than 20 μm (282863; Sigma-Aldrich), as needed to simulate acoustic scattering similar to that of arteries; and 4) 0.3% potassium sorbate (85520; Sigma-Aldrich), which served as an antimicrobial agent. The mixture was prepared in solution form at 90 °C temperature under a double-boiler configuration. It was left to cool and settle for at least 12 h to foster mixture degassing.

2) *Vessel Wall Casting Procedure*: In the first step of the actual vessel tube construction process, a vessel core was mounted onto the fixture slots of the outer mold. Next, the two mold halves were sandwiched together and were sealed with coated polyethylene tape; in doing so, the vessel core was suspended within the enlarged bifurcation void of the outer mold. Afterward, using a 150-mL syringe, the vessel mimicking mixture was slowly injected into the inlet runner duct of the mold to fill the cavity between the vessel core and the enlarged bifurcation void [see Fig. 4(a)]. The mixture injection was performed until there was overflow at the outlet vents of the mold and gaseous bubbles were vented out. Three freeze-thaw cycles were subsequently administered to the entire outer mold. In each cycle, two operations were performed in sequence: 1) placing the mold in a -20 °C chest freezer for 24 h (to solidify the vessel mimicking mixture and, in turn, allow the PVA molecules to form polymer crystallites) and 2) thawing the mold at 4 °C for 24 h (to allow the PVA crystallites to form porous networks and, in turn, develop elastic wall characteristics).

3) *Vessel Core Removal*: After an elastic vessel wall was formed around the vessel core, it was taken out of the outer mold for further processing. In particular, the vessel core was removed to obtain an elastic vessel tube with hollow lumen. This step was conducted by gently snapping the vessel core to crack its mechanical structure and slowly retrieving the PLA fragments. The vessel lumen was then flushed with degassed

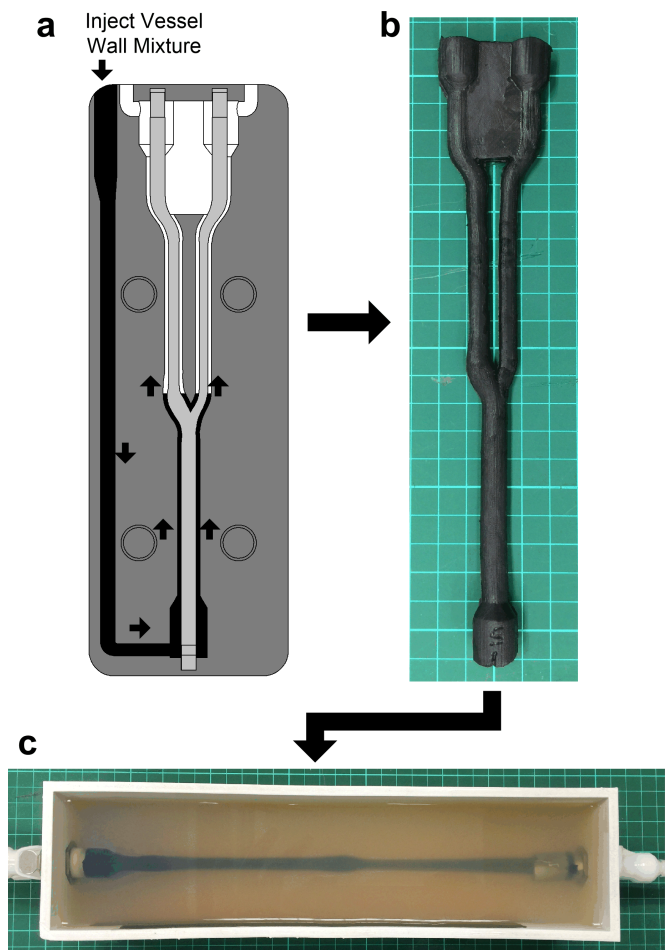


Fig. 4. Vessel tube construction in the new phantom protocol. (a) Vessel wall casting is achieved by injecting vessel mimicking mixture through the inlet runner duct into the wall cavity in the outer mold. (b) Photograph of the fabricated vessel wall tube after three freeze-thaw cycles (with vessel core removed). (c) Top-down view of the completed carotid bifurcation phantom with the vessel tube mounted onto the phantom box and the congealed tissue mimicking slab.

water to rinse out remaining PLA debris. A photograph of the completed vessel tube is shown in Fig. 4(b). It should be pointed out that the outer mold can be readily reused to fabricate vessel tubes using other PLA vessel cores.

D. Phantom Assembly

1) *Phantom Box Construction*: To facilitate mounting of the fabricated bifurcation vessel tube, an open box with an inner dimension of $240 \times 70 \times 60$ mm³ and a side thickness of 5 mm was built using a similar CAD drafting and 3-D printing procedure as that used for the design of vessel core and outer mold. For this open box, three quick-fit flow connectors (EW-06361-61; Cole-Parmer, Vernon Hills, IL, USA) were installed onto the inlet and outlet sides to accommodate the three branch ends of the bifurcation vessel tube. These connectors were aligned in vertical coplanar orientation in parallel to the central long-axis plane of the bifurcation geometry. A 5-mm-thick acoustic absorbing rubber was also sealed to the inner bottom side of the box to suppress pulse reflections from the box base during imaging operations.

2) *Vessel Tube Mounting*: The three ends of the fabricated hollow vessel tube were snapped onto the corresponding flow connectors on the phantom box. To maintain the lumen geometry following vessel tube mounting, degassed water was gently pumped into the vessel lumen through the inlet connector, while the two outlet connectors were sealed. This step was essential to prevent the vessel from collapsing when forming the tissue mimicking slab.

3) *Tissue Mimicking Slab*: An agar-gelatin mixture was prepared to form an elastic tissue mimicking slab for the phantom. The mixture formula was composed of (by weight): 1) 94.45% distilled water; 2) 1.5% agar (A1296; Sigma-Aldrich); 3) 3.75% gelatin (G2500; Sigma-Aldrich); and 4) 0.3% potassium sorbate preservatives. This mixture was made in solution form at 90 °C temperature. After cooling it to 45 °C, it was poured into the open volume of the phantom box, and it was allowed to set in room temperature for 6 h to form a congealed slab [see Fig. 4(c)]. The box was stored inside a 4 °C fridge prior to use in imaging experiments.

III. PHANTOM MATERIAL PROPERTY MEASUREMENTS

A. Elastic Properties

For the vessel wall material and the tissue mimicking material of our fabricated phantoms, their mechanical strength was gauged through a uniaxial tensile test protocol that we have used previously to characterize compliant photopolymers [32]. This analysis was conducted using a series of dumbbell-shaped test strips that were casted as follows. First, a set of dumbbell strip negative molds were made using CAD and 3-D printing; each mold cavity was 61 mm in total length, $20 \times 10 \times 2 \text{ mm}^3$ in size at the center, and $16 \times 30 \times 22 \text{ mm}^3$ in size at the two machine gripping ends. Second, using these molds, we created 30 test strips from the vessel mimicking mixture and the tissue mimicking mixture (i.e., the same contents as those used for phantom fabrication); they, respectively, underwent three-stage freeze-thaw cycles (to form the vessel wall) and 6-h congealing period (to form the tissue slab). These test strips were then mounted one at a time onto a 2-kN-load tensile tester (5848; Instron, Norwood, MA, USA), and they each underwent an elongation test to obtain load-extension curves as described earlier [32]. Stress-strain curves were derived from the acquired data using MATLAB, and the slope of each curve corresponded to the elastic modulus of a sample.

Fig. 5(a) shows the stress-strain curves of all 30 test strip realizations for the vessel wall and the tissue mimic. These test data indicate that both materials exhibited a linear stress-strain relation. As summarized in Fig. 5(b), the elastic modulus of the vessel wall was found to be 106.1 kPa (± 3.6 kPa), while that for the tissue mimic was 35.9 kPa (± 6.0 kPa). Note that the vessel wall had a higher elastic modulus than the tissue mimic, as aligned with previously published data [46].

B. Acoustic Properties

The acoustic speed and attenuation coefficient of the vessel wall material and the tissue mimicking material were gauged using the same insertion-based measurement technique applied

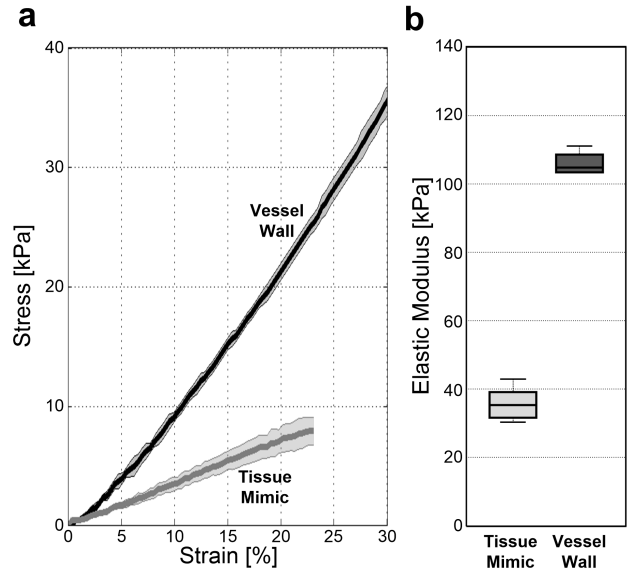


Fig. 5. Elastic property analysis for the vessel wall and the tissue mimic. (a) Stress-strain curves derived from uniaxial tensile testing. Each line indicates the mean over 30 samples. The upper and lower bounds around the mean line denote the standard deviation. (b) Box-whisker plots of the calculated elastic moduli for the two materials. Error bars denote the smallest and largest values in the 30-sample data set.

in our prior study on compliant photopolymers [32]. In brief, the setup involved an aligned 10-cm-spaced pair of water-immersed 5-MHz piston transducers (C567-SM; Olympus NDT, Waltham, MA, USA). One transducer was used for pulse transmission, as driven by a waveform generator (33120A; Agilent Technologies, Palo Alto, CA, USA). The other was used for reception, whose detected signals were conditioned via a pulse receiver (5800PR; Olympus), and the output was fed into an oscilloscope (DSO5014A; Agilent).

To facilitate acoustic property measurements, we prepared rectangular test slabs with four different thicknesses (2, 4, 6, and 8 cm). These slabs were made using a similar procedure as that used to make the test strips for our mechanical tests (with the exception that the molds were redesigned to take into account the new test slab dimensions). A total of 30 test slab batches were each made for the vessel wall material and tissue mimicking material. Using these samples, we applied the time-of-flight method [47] to estimate the acoustic speed, similar to what we did earlier [32]. Also, we adopted the amplitude thickness regression method as described by others [31] to derive the attenuation coefficient; for these measurements, we performed a frequency sweep from 3 to 7 MHz at 0.1-MHz increments, and narrowband pulses (20-cycle duration) were used. In estimating the attenuation coefficient, we assumed linear frequency dependence in line with published data [46].

The experimentally derived acoustic property values are listed in Table I for the vessel wall and the tissue mimic. It is worth noting that the average acoustic speed for the two materials (vessel wall: 1535 m/s; tissue mimic: 1510 m/s) was close to the nominal speed of 1540 m/s for human tissue. As well, the average acoustic attenuation coefficient values measured for the two materials [vessel wall: 0.229 dB/(cm · MHz);

TABLE I
ACOUSTIC PROPERTIES OF MATERIALS USED IN PHANTOM FABRICATION

Parameter	Tissue mimic	Vessel wall
Acoustic speed, c_o (m/s)	1510 ± 1.3	1535 ± 2.4
Attenuation coefficient, α [dB/(cm·MHz)]	0.145 ± 0.027	0.229 ± 0.032

* Mean \pm standard deviation (30 samples)

tissue mimic: 0.145 dB/(cm · MHz)] were found to be low. This shows that the materials used in our phantom fabrication process exhibit strong acoustic compatibility for use in ultrasound imaging experimentation.

IV. IMAGING EXPERIMENTATION

A. Flow Circuit Assembly

The carotid bifurcation phantoms developed using our new protocol were used in a series of imaging experiments that sought to analyze vessel motion and flow dynamics. In each experimental trial, a phantom was first connected to a flow circuit that comprised the same components as those used in [32]. Briefly, the phantom's CCA inlet branched was plugged into a gear pump system (AccuFlow-Q; Shelley Medical Imaging, London, ON, Canada) through flexible vinyl flow tubing (EW-96480-04; Cole Parmer). At its ECA and ICA outlet branches, there were 2-mm-diameter flow resistors placed in between the flow outlet and the return route to the flow pump reservoir. The blood mimicking fluid was a nylon scatterer solution (BMF-US; Shelley Medical Imaging) whose acoustic and viscous properties are matched to that of human blood [48]. During operation, a carotid pulse waveform with 1.2-Hz frequency (i.e., 72 beats/min) was generated using the gear pump. The mean and systolic pump output were, respectively, 1.95 and 6.5 mL/s.

B. Initial Experimentation With Clinical Scanner

To confirm the compatibility of our phantoms from an ultrasound imaging standpoint, we used the clinical mode of a SonixTouch scanner (Analogic Ultrasound, Peabody, MA, USA) to acquire color flow images using the conventional scanline-based imaging paradigm. The transducer that we used was an L14-5 linear array (Analogic) with 128 elements and 0.3048-mm pitch. The center frequency, pulse repetition frequency (PRF), and pulse duration were, respectively, set to 5 MHz, 3.3 kHz, and 3 cycles. Also, the following parameters specific to scanline-based color flow imaging were used: 1) transmit focus—3 cm depth; 2) number of lines—128; 3) number of firings per line—10; and 4) wall filter cutoff—100 Hz.

As reference data, Fig. 6 shows clinical color flow image frames taken during the systolic phase of a pulse cycle for different bifurcation phantom geometries. It is worth noting that, for these walled phantoms, all three carotid bifurcation branches can be visualized in clinical color flow imaging as similar to that for wall-less phantoms, and a flow jet appeared

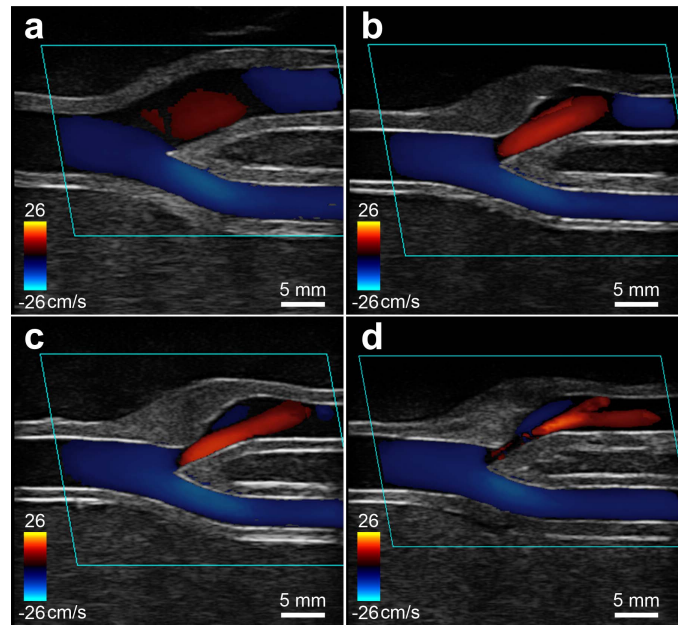


Fig. 6. Clinical color flow image frames at pulse systole for four carotid bifurcation phantoms produced using our new protocol. (a) Healthy model (no stenosis). Diseased models with different extents of eccentric stenosis at the ICA inlet (b) 25%, (c) 50%, and (d) 75%. Note that the maximum velocities shown in the color bar have no angle correction (impossible to correct due to varying Doppler angle in the imaging view). The dark region at the construction site in (d) was a wraparound artifact due to aliasing.

at the ICA inlet of stenosed geometries as expected [30]. This finding shows that our new phantom design protocol can indeed produce walled phantoms with strong compatibility with ultrasound imaging. Such a technical feature is difficult to achieve with previous design protocols for walled carotid bifurcation phantoms [31], [32] and commercially available carotid bifurcation flow phantoms.

C. Plane Wave Imaging Experimental Platform

The wall and flow dynamics of our phantoms were imaged and analyzed using our group's research-purpose ultrasound imaging platform that comprised a reconfigured transmit pulser based on the research mode of our SonixTouch scanner and a channel-domain raw data acquisition unit [49]. The transmit pulser was programmed to operate in unsteered plane wave transmission mode by specifying all array elements to fire simultaneously [41]. The center frequency, PRF, and pulse duration were set to 5 MHz, 5 kHz, and 3 cycles, respectively. In each realization of data acquisition, the transducer scan plane was first aligned to the parallel central long-axis view of the phantom, and raw channel-domain data were acquired over all 128 array elements up to 5-cm depth on a consecutive basis until the hardware's on-board data buffer was filled. Note that our system had 16 GB of random access memory; for 5-cm depth, this memory buffer was sufficient to store raw data for 2.5 s with 40-MHz sampling rate and 12-bit sampling resolution. The acquired channel raw data were subsequently streamed offline to our graphical processing unit (GPU) computing platform [50] for processing, where the steps of analytic signal conversion as well as delay and sum were carried out

to form frames of analytic data on a pixel-by-pixel basis (with $0.2 \text{ mm} \times 0.2 \text{ mm}$ pixel dimension) using our previously established GPU-based beamformer [51]. Doppler analysis was then performed using MATLAB (MathWorks, Inc., Natick, MA, USA) on the resulting image frames, as described in Sections IV-D to IV-F.

D. Wall Motion Dynamics Analysis

To characterize the extent of vessel wall motion in our phantoms, we performed pulse wave propagation analysis in the CCA branch where the geometry was by and large a straight tube regardless of the stenosis level in the ICA branch. For this task, we first defined a lateral strip (1-mm axial thickness; 10-mm lateral width) along the proximal wall center of the CCA branch (4 mm away from the bifurcation point). Next, we formed an array of slow-time ensembles corresponding to different lateral positions (in 0.2-mm lateral steps) as retrieved from the analytic data frame stack. For the slow-time ensemble at each position, we estimated the wall velocity waveform by: 1) applying a low-pass filter (minimum order equiripple design with 0.05 normalized cutoff; 125th order for our parameters to ensure a sharp cutoff at the specific frequency) to suppress unwanted blood echoes that may exhibit high Doppler frequency characteristics; 2) executing the lag-one autocorrelation phase algorithm [52] with a 64-sample sliding window implementation and converting the resulting phase estimates into velocity via the Doppler equation. Subsequently, the mean wall velocity waveform for each lateral position was computed by averaging the estimated velocities over the 1-mm axial range at that lateral position. The pulse wave velocity was then estimated by first finding, at each lateral position, the time when the wall velocity magnitude waveform first reached 0.01-cm/s axial velocity after the cusp (to denote as the pulse arrival instance) that signifies the start of significant wall motion. These pulse arrival times were subsequently plotted as a function of lateral position, and the resulting slope, which theoretically corresponds to pulse wave velocity [53], was computed.

For our walled carotid bifurcation phantoms, the CCA wall velocity waveforms at different lateral positions (derived in parallel through plane wave imaging) exhibited temporal shifts that are characteristic of pulse wave propagation along the vessel wall. This finding is illustrated in Fig. 7, which shows a series of CCA wall velocity waveforms derived from the diseased bifurcation model with 50% stenosis. As can be observed, there is a progressive shift in the pulse arrival time from the proximal to the distal side of the lateral strip [Fig. 7(a) and (b)]. The pulse arrival time at the proximal and distal ends of the lateral strip was estimated to be 74 and 76 ms, respectively. The shift trend was generally linear, and the pulse wave velocity was found to be 4.25 m/s [Fig. 7(c)].

Similar results were obtained in the CCA of the other bifurcation phantoms that we fabricated. The pulse wave velocity estimates for the four bifurcation phantoms developed in this paper were found to range between 4.0 and 5.63 m/s (mean: 4.67 m/s; standard deviation: 0.71 m/s). Note that

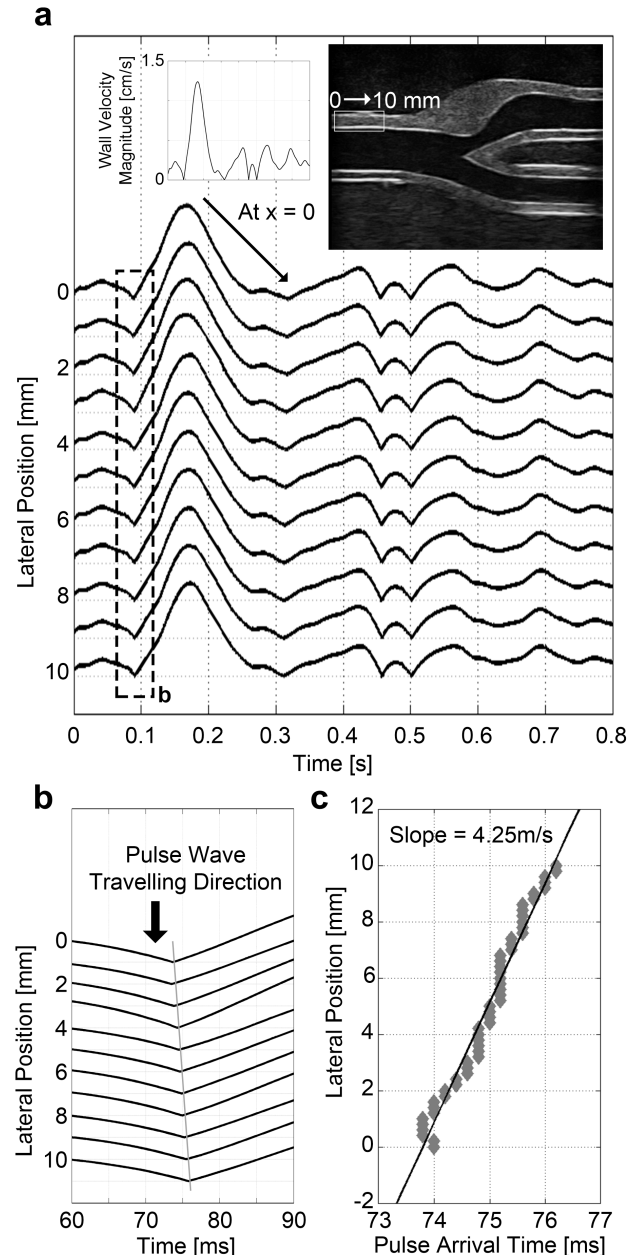


Fig. 7. Pulse wave propagation along the CCA proximal wall of the healthy bifurcation phantom. (a) Stacked plot of wall velocity magnitude waveforms at different lateral positions of a 10-mm strip as indicated in the B-mode reference image. Maximum wall velocity was 1.3 cm/s. (b) Enlarged window that shows the first wall velocity waveform cusp (denoted by pulse arrival time) shifting temporally from proximal to distal end of lateral strip. (c) Plot of pulse arrival time as a function of lateral position on the CCA proximal wall, with a slope of 4.25 m/s that equals the pulse wave velocity.

these estimates generally matched the elastic property of the wall material. This trend was confirmed by comparing the estimated pulse wave velocity values against the nominal one calculated using the modified Moens-Korteweg equation that waived the thin wall assumption in the classical formula [54]. For our phantom parameters (106.1-kPa elastic modulus; 1.5-mm wall thickness; 6-mm CCA diameter; 1037-kg/m^3 blood mimicking fluid density), the estimated values were found to range between 90% and 125% of the nominal value of 4.5 m/s.

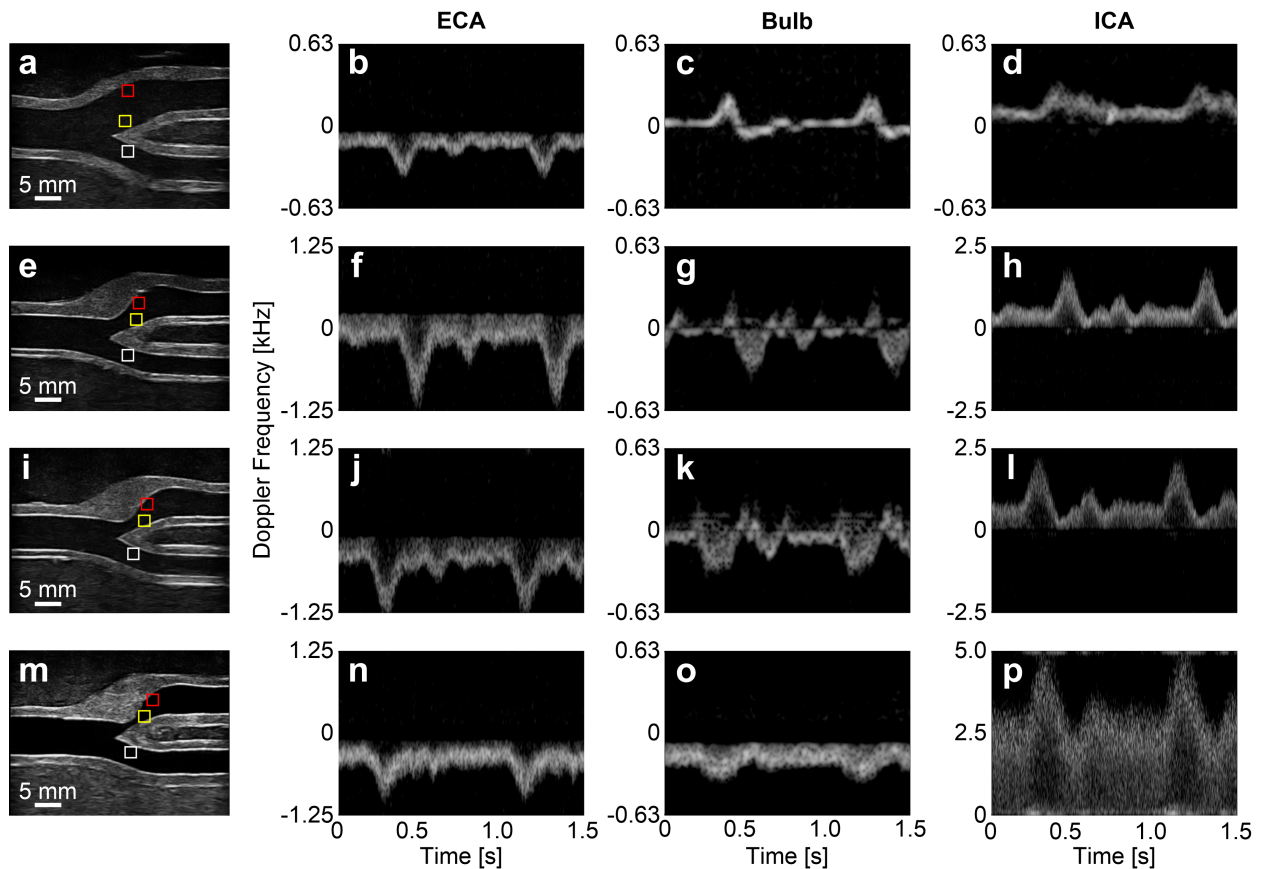


Fig. 8. Multigate plane wave spectral Doppler analysis of flow dynamics in the carotid bifurcation phantoms produced using our new protocol. First column: B-mode reference images for (a) healthy bifurcation and diseased bifurcation with ICA eccentric stenosis of (e) 25%, (i) 50%, and (m) 75%. Range gate locations used for Doppler spectrogram computation are marked by three colored boxes: (white) ECA inlet, (red) carotid bulb, and (yellow) ICA inlet. Second, third, and fourth columns: Spectrograms at the ECA inlet, carotid bulb, and ICA inlet for the four bifurcation geometries, arranged in the same order as that in the first column.

E. Multigate Spectral Doppler Analysis

To assess whether the flow patterns produced in our phantoms were aligned with the spatiotemporal dynamics observed with particle image velocimetry [33], [34], a series of Doppler spectrograms was derived from multiple $1 \text{ mm} \times 1 \text{ mm}$ range gates in the imaging view. Such a multigate spectral Doppler analysis was performed concurrently for each data set; it was achievable because the slow-time data for all pixel positions were acquired simultaneously when the plane wave imaging paradigm was used (i.e., unlike conventional spectral Doppler analysis that can take place only at a single range gate) [41]. To conduct this flow signal analysis, we first extracted the set of raw slow-time ensembles for each $1 \text{ mm} \times 1 \text{ mm}$ range gate by extracting data from the corresponding pixel positions in the analytic data frame stack. Next, we applied a high-pass filter (minimum order equiripple design with 0.05 normalized cutoff; 135th order for our parameters) to suppress unwanted tissue clutter in each slow-time ensemble. Afterward, Doppler spectrograms were computed from the filtered slow-time data using a sample window size of 64 (with Hamming tapering) and a sliding step size of two. The resulting Doppler spectrogram for each range gate was obtained by compounding the Doppler spectrogram of all the slow-time ensembles within the specified range gate. For those range

gates with low Doppler frequency components (attributed to slower flow), we downsampled the slow-time data by a factor of two or four (i.e., reducing the PRF to 2.5 or 1.25 kHz) to improve the Doppler resolution and in turn better detect these low-frequency components.

Using multigate plane wave spectral Doppler analysis, we found that the flow dynamics within the vessel lumen of our developed phantoms generally matched the expected flow profile for coplanar carotid bifurcation geometries [33], [34]. The corresponding data are shown in Fig. 8, which shows a series of Doppler spectrograms for healthy (first row) and diseased bifurcation phantoms (second, third, and fourth rows) at three range gate locations: ECA inlet (second column), carotid bulb (third column), and ICA inlet (fourth column).

Three points of interest can be noted from Fig. 8. First, at the ECA inlet, since there was no stenotic narrowing, the Doppler spectrogram resembled a typical carotid pulse pattern (with a main systolic peak and a diastolic notch) for all the bifurcation geometries considered [Fig. 8(b), (f), (j), and (n)]. It should be pointed out that the Doppler frequencies were negative at the ECA inlet since flow was moving away from the transducer.

The second point worth noting from Fig. 8 is that the Doppler spectrograms at the carotid bulb revealed differences in flow pattern as the extent of stenosis increased. In particular,


while quadphasic flow was observed in the carotid bulb of the healthy bifurcation [Fig. 8(c)], a multiphasic flow pattern was observed for the diseased bifurcation phantoms with mild stenosis levels of 25% and 50% [Fig. 8(g) and (k)]. This trend is an indication of increased flow disturbance in the carotid bulb as stenotic plaque began to develop. In contrast, at higher level of stenosis (75%) [Fig. 8(o)], a monophasic flow pattern, as indicative of unidirectional flow locally, can be observed in the carotid bulb.



The third observation of interest in Fig. 8 is that, at the ICA inlet, the Doppler spectrograms showed a progressive increase in peak systolic Doppler frequency as the stenosis percentage increased. In the healthy bifurcation, a maximum Doppler frequency of 350 Hz was observed over a pulse cycle [Fig. 8(d)]. In the presence of stenotic narrowing, this value has gradually increased to 1818, 2247, and 4860 Hz, respectively, for 25% [Fig. 8(h)], 50% [Fig. 8(l)], and 75% [Fig. 8(p)] stenosis levels. This trend is, after all, characteristic of flow jets that arise at the site of stenosis.


F. Integrative Imaging of Wall Motion and Flow Dynamics

To demonstrate the feasibility of using our phantoms in integratively tracking wall motion and flow patterns, we have concurrently performed the following on the image frame stack formed from each phantom data set: 1) tissue Doppler mapping of vessel wall motion; 2) color-encoded speckle imaging of bifurcation flow dynamics [30]. This integrative imaging work was conducted by first manually segmenting the boundaries of vessel wall and flow region using a built-in contour function (roipoly) in MATLAB. For those pixels inside the vessel wall, the same low-pass filtering and lag-one autocorrelation phase algorithm as that described in Section IV-D was applied to compute the local wall velocities. The results were then color coded using a cyan color map with brightness pegged to the wall velocity magnitude, and an *ad hoc* mean-and-median filtering routine was applied to remove spurious color codes. To better highlight the spatiotemporal onset of a wall motion cycle within a pulse period, low wall velocity estimates below 0.01 cm/s were color coded using a magenta color instead of cyan. This visualization strategy was applied only to the proximal wall (extends from CCA to ICA) so as to render differences in pulse wave propagation through healthy and diseased bifurcation geometries, the latter of which has a thickened plaque at the proximal wall of the ICA inlet. On the other hand, for those pixels inside the flow region, we applied the same flow speckle and flow velocity estimation procedure that was used in our previous work [30]. The bifurcation flow dynamics were then rendered in a duplex style by concurrently displaying, via alpha compositing, both flow speckles and velocity color codes that were pegged to a hot-cold color map. This duplex flow visualization and the wall motion visualization were overlaid on top of the corresponding B-mode image frame for integrative display, and the results were rendered in cine loop form over the acquired image frame stack.

Integrative imaging of vessel wall motion and blood flow using plane wave excitation principles was found to be capable of rendering differences in the pulsation behavior of healthy

and diseased bifurcation phantoms that we developed. As a cine loop illustration of this finding, Movie 1  compares the dynamics of wall motion and blood flow (playback rates: normal–250 frames/s; slow motion–50 frames/s) at different phases of the pulse cycle in the healthy carotid bifurcation (top window) and in the 50% stenosed bifurcation (middle window). Note that, in this cine loop, a Doppler spectrogram taken at the ICA inlet was shown (bottom window) to provide reference to the pulse phase as images were rendered. To provide a still-frame rendering of this cine loop, image frames at key time points with distinct wall motion or flow features are extracted and are plotted in Fig. 9.

One key dynamic event that is visualized in Movie 1  and Fig. 9 is the difference in pulse wave propagation dynamics in the healthy and diseased bifurcation phantoms. Pulse wave fronts are identified as the +0.01 cm/s wall velocity upstroke and denoted with a color-coded transition from magenta to cyan. As rendered in the slow motion playback of Movie 1  (0–4.5 s), although the pulse wave arrived in the CCA proximal wall at the same time for both bifurcation geometries [Fig. 9(b) and (i)], it propagated through the healthy bifurcation at a slower speed [Fig. 9(c)–(e)] than the 50% stenosed bifurcation [Fig. 9(j)–(l)]. Pulse wave propagated through the imaging view for the 50% stenosed model in 8.8 ms, while an additional 3.2 ms was required for the pulse wave to propagate a similar segment of the healthy model. This is in line with the clinical expectation of pulse wave velocity to be faster in a diseased model. It is also worth noting that the pulse wave propagated through the carotid bifurcation before flow systole commenced. In other words, pulse wave and flow systole are asynchronous events in a pulsatile flow cycle.

Further signs of time lag between peak wall motion and systolic flow can be found from Fig. 9(f) and (m), as well as the presystolic frames of Movie 1 . As can be observed, prior to flow systole, the vessel wall underwent the fastest motion (with 1.5-cm/s wall velocity). In contrast, at flow systole, where the fastest flow speeds were detected [Fig. 9(g) and (n)], the corresponding wall velocity became slower. Such a fluid-structure interaction relationship is in agreement with findings from previous work on simultaneous imaging of wall and flow dynamics [14].

V. DISCUSSION

A. Summary of Methodological Contributions

The carotid artery is well regarded as a major application domain of vascular ultrasound. Accordingly, designing anatomically realistic carotid phantoms to facilitate vascular imaging investigations has long been a research topic of practical interest [25], [26]. Nonetheless, previous endeavors (including commercial ones) have only had mixed success in fabricating walled carotid phantoms, as their acoustic compatibility is rather limited [31], [32]. In this paper, we have established a novel walled phantom fabrication protocol that can overcome the technical limitations of previous solutions, and we have made use of this protocol to achieve, to the best of our knowledge, the first successful design of walled carotid bifurcation phantoms that are acoustically compatible with

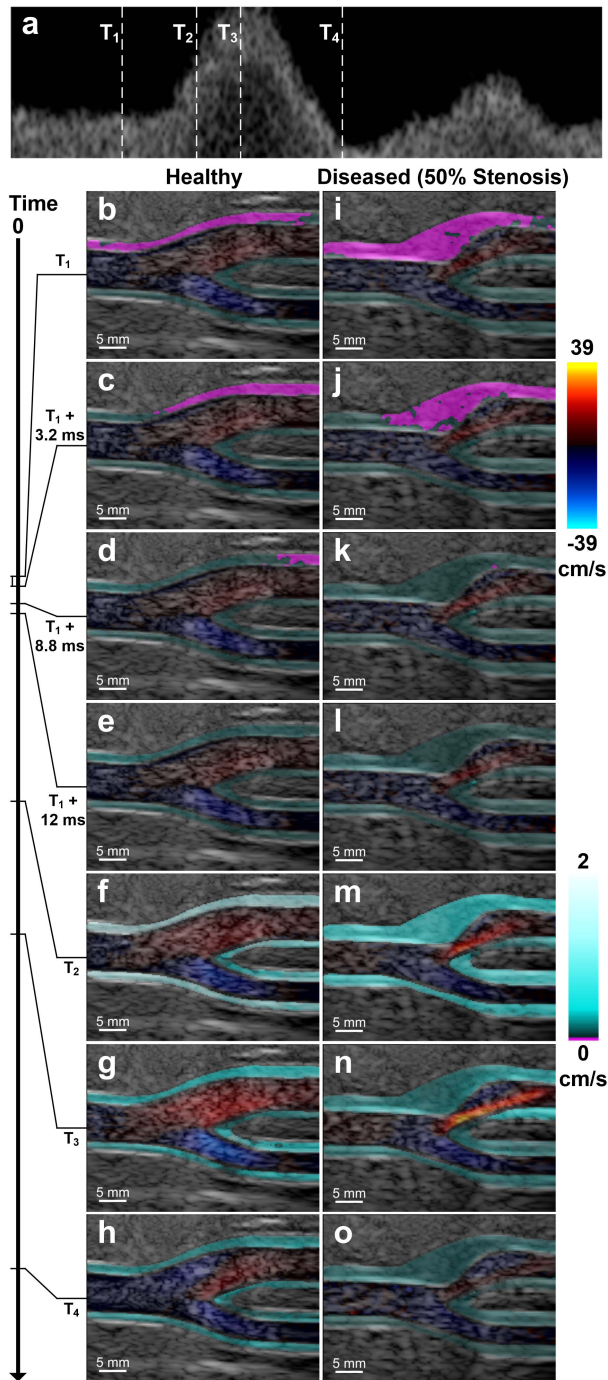


Fig. 9. Plane wave image series integratively showing vessel wall motion and color-encoded flow speckle dynamics. (a) Doppler spectrogram taken at the ICA inlet, with key time points marked. Representative image frames are shown for two phantoms (b)–(h) healthy bifurcation and (i)–(o) diseased bifurcation with 50% ICA eccentric stenosis. The hues of red-blue and cyan-magenta are, respectively, used to depict flow velocity and wall velocity magnitude.

ultrasound imaging (Table I) and whose vessel wall has a similar elasticity as that of human arteries (Fig. 5). Our solution uses CAD tools and 3-D printing technology to directly build vessel cores (Fig. 2) and create outer molds (Fig. 3), which are then leveraged to efficiently cast vessel tubes (Fig. 4). From an operational standpoint, this new protocol can be considered as more efficient and less skill demanding than

previous walled phantom fabrication attempts that required the use of low melting point alloys to form vessel cores and the creation of multiple molds to achieve separate casting of vessel cores and vessel tubes [31], [38], [39]. It also differs from [32] that sought to directly build vessel tubes through rapid prototyping of compliant photopolymer materials whose properties cannot be controlled. It is worth pointing out that the phantom materials used in our fabrication protocol may be inferred to be mechanically stable over time, as they were similar in contents with those used by others and were deemed to be stable over a seven-month period (for both agar-gelatin tissue mimic [55] and PVA vessel mimic [56]). Also, although our tissue mimic and vessel wall have a slightly lower attenuation coefficient compared with those *in vivo*, material attenuation can be readily adjusted by fine-tuning the graphite concentration in the vessel and tissue mimic solution [57].

B. Feasibility of Conducting Imaging Experimentation Using Our New Bifurcation Phantoms

Besides methodological innovations in carotid phantom design, we have also provided the first demonstration on using our walled carotid phantoms to facilitate experimentation of clinical color flow imaging (Fig. 5) as well as emerging techniques (namely, plane wave imaging, a paradigm that has garnered interest in the ultrasound community in recent years [41]). In our plane wave imaging experiments, our phantoms were found to produce vessel wall motion dynamics that were in agreement with pulse wave propagation in an elastic vessel wall (Fig. 7), and their flow dynamics generally matched the expected patterns in the carotid bifurcation (Fig. 8). More importantly, we demonstrated integrative tracking of vessel wall motion and blood flow dynamics within our phantoms using plane wave imaging, and have gained initial insight into the fluid-structure interaction differences between healthy and diseased bifurcation phantoms (Movie 1 and Fig. 9). These findings serve to attest that the set of walled bifurcation phantoms developed with our new protocol can be applied to longitudinal analysis of the performance of vascular imaging methods that individually or integratively assess wall motion and blood flow dynamics.

The discrepancy in the estimated values of pulse wave velocity from its nominal value may be attributed to a combination of factors. First, the analysis performed in our study measured the pulse wave velocity at the CCA over a short segment (10-mm lateral width) and consequently introduced considerable measurement variations. Second, our estimation method is prone to the influence of pulse wave reflections due to the geometrical variations of the bifurcation phantom. Pulse wave reflection occurs in scale with the mismatch between characteristic impedance of the artery, mainly at discontinuities of the arterial system in side branches and arterial stiffening [58]. In our case, pulse reflection may occur at the branching site, as well as the stenosed region, leading to potential estimation bias. Third, several imaging parameters such as frame rate and spatial resolution, as well as noise such as motion artifact are known to affect the accuracy and precision of pulse wave velocity measurements [59].

C. Perspectives for Further Development

It is worth noting that our new phantom fabrication protocol may be extended to develop carotid bifurcation phantoms with different vessel wall stiffness as they may appear in aging vessels and diseased arteries with stenotic narrowing. In particular, the elastic modulus of the vessel wall may be tuned by either: 1) adjusting the PVA concentration used for the vessel wall mixture and/or 2) modifying the duration and repetition of the freeze-thaw cycle process. Accordingly, a set of carotid phantoms with the same geometry but varying vessel wall stiffness could be readily fabricated to reconstruct the fluid-structure interactions of aging vasculature that is known to lead to arterial stiffening. This alternate set of phantoms can be used toward developing new vascular imaging methods that seek to assess vascular aging. Expanding beyond such a concept, it is also possible to apply our phantom fabrication protocol to establish a bivariate library of carotid bifurcation phantoms with varying wall stiffness and stenosis levels. Such a phantom library would help researchers gain integrative insight into whether new vascular imaging methods can effectively identify fluid-structure interaction differences at various stages of atherosclerosis and vascular aging. In addition, it is worth exploring the fabrication of vessel phantoms with anisotropic properties to more precisely resemble the physiological features of biological vessels. Such features can be achieved by embedding elastic Spandex fibers into the PVA cryogel [60].

VI. CONCLUSION

Properly designing carotid bifurcation phantoms and demonstrating their use in vascular ultrasound investigations are important to drive technical developments in carotid diagnostics. The new phantom design protocol that we have reported in this paper is expected to foster such developments. Indeed, the walled nature of our developed phantoms makes them versatile for use in vessel wall imaging, flow imaging, and integrative imaging of wall motion and flow dynamics.

ACKNOWLEDGMENT

The authors would like to thank Paul J. B. Kuan for his technical assistance on laboratory work and related fabrication processes.

REFERENCES

- [1] W. M. Nichols, M. F. O'Rourke, and C. Vlachopoulos, *McDonald's Blood Flow in Arteries: Theoretical, Experimental and Clinical Principles*, 6th ed. Boca Raton, FL, USA: CRC Press, 2012.
- [2] Y. Jiang, K. Kohara, and K. Hiwada, "Association between risk factors for atherosclerosis and mechanical forces in carotid artery," *Stroke*, vol. 31, no. 10, pp. 2319–2324, Oct. 2000.
- [3] C. Slager, J. Wentzel, F. Gijzen, J. Schuurbiens, A. van der Wal, A. van der Steen, and P. Serruys, "The role of shear stress in the generation of rupture-prone vulnerable plaques," *Nature Rev. Cardiol.*, vol. 2, no. 8, pp. 401–407, Aug. 2005.
- [4] C. Cheng, "Atherosclerotic lesion size and vulnerability are determined by patterns of fluid shear stress," *Circulation*, vol. 113, no. 23, pp. 2744–2753, Jun. 2006.
- [5] C. L. de Korte, H. H. G. Hansen, and A. F. W. van der Steen, "Vascular ultrasound for atherosclerosis imaging," *Interface Focus*, vol. 1, no. 4, pp. 565–575, Jun. 2011.
- [6] P. R. Hoskins, "Haemodynamics and blood flow measured using ultrasound imaging," *Proc. Inst. Mech. Eng. H, J. Eng. Med.*, vol. 224, no. 2, pp. 255–271, Feb. 2010.
- [7] P. Kruizinga, F. Mastik, S. C. H. van den Oord, A. F. L. Schinkel, J. G. Bosch, N. de Jong, G. van Soest, and A. F. W. van der Steen, "High-definition imaging of carotid artery wall dynamics," *Ultrasound Med. Biol.*, vol. 40, no. 10, pp. 2392–2403, Oct. 2014.
- [8] S. Salles, A. J. Y. Chee, D. Garcia, A. C. H. Yu, D. Vray, and H. Liebgott, "2-D arterial wall motion imaging using ultrafast ultrasound and transverse oscillations," *IEEE Trans. Ultrason., Ferroelectr., Freq. Control*, vol. 62, no. 6, pp. 1047–1058, Jun. 2015.
- [9] K. Hansen, J. Udesen, F. Gran, J. A. Jensen, and M. B. Nielsen, "In-vivo examples of flow patterns with the fast vector velocity ultrasound method," *Ultraschall Med.*, vol. 30, no. 5, pp. 471–477, Oct. 2009.
- [10] B. Y. S. Yiu, S. S. M. Lai, and A. C. H. Yu, "Vector projectile imaging: Time-resolved dynamic visualization of complex flow patterns," *Ultrasound Med. Biol.*, vol. 40, no. 9, pp. 2295–2309, Sep. 2014.
- [11] P. Tortoli, T. Morganti, G. Bambi, C. Palombo, and K. V. Ramnarine, "Noninvasive simultaneous assessment of wall shear rate and wall distension in carotid arteries," *Ultrasound Med. Biol.*, vol. 32, no. 11, pp. 1661–1670, Nov. 2006.
- [12] H. Hasegawa and H. Kanai, "Simultaneous imaging of artery-wall strain and blood flow by high frame rate acquisition of RF signals," *IEEE Trans. Ultrason., Ferroelectr., Freq. Control*, vol. 55, no. 12, pp. 2626–2639, Dec. 2008.
- [13] I. K. Ekroll, A. Swillens, P. Segers, T. Dahl, H. Torp, and L. Lovstakken, "Simultaneous quantification of flow and tissue velocities based on multi-angle plane wave imaging," *IEEE Trans. Ultrason., Ferroelectr., Freq. Control*, vol. 60, no. 4, pp. 727–738, Apr. 2013.
- [14] J. Luo and E. E. Konofagou, "Imaging of wall motion coupled with blood flow velocity in the heart and vessels in vivo: A feasibility study," *Ultrasound Med. Biol.*, vol. 37, no. 6, pp. 980–995, Jun. 2011.
- [15] P. R. Hoskins, "Simulation and validation of arterial ultrasound imaging and blood flow," *Ultrasound Med. Biol.*, vol. 34, no. 5, pp. 693–717, May 2008.
- [16] W. Dabrowski, J. Dunmore-Buyze, R. N. Rankin, D. W. Holdsworth, and A. Fenster, "A real vessel phantom for imaging experimentation," *Med. Phys.*, vol. 24, no. 5, pp. 687–693, May 1997.
- [17] W. Dabrowski, J. Dunmore-Buyze, H. N. Cardinal, and A. Fenster, "A real vessel phantom for flow imaging: 3-D Doppler ultrasound of steady flow," *Ultrasound Med. Biol.*, vol. 27, no. 1, pp. 135–141, Jan. 2001.
- [18] J. Bale-Glickman, K. Selby, D. Saloner, and O. Savaş, "Experimental flow studies in exact-replica phantoms of atherosclerotic carotid bifurcations under steady input conditions," *J. Biomech. Eng.*, vol. 125, no. 1, pp. 38–48, Jan. 2003.
- [19] R. K. Warriner, K. W. Johnston, and R. S. C. Cobbold, "A viscoelastic model of arterial wall motion in pulsatile flow: Implications for Doppler ultrasound clutter assessment," *Physiol. Meas.*, vol. 29, no. 2, pp. 157–180, Feb. 2008.
- [20] S. Balocco, O. Bassot, J. Azencot, P. Tortoli, and C. Cachard, "3D dynamic model of healthy and pathologic arteries for ultrasound technique evaluation," *Med. Phys.*, vol. 35, no. 12, pp. 5440–5450, Dec. 2008.
- [21] A. Swillens, J. Degroote, J. Vierendeels, L. Lovstakken, and P. Segers, "A simulation environment for validating ultrasonic blood flow and vessel wall imaging based on fluid-structure interaction simulations: Ultrasonic assessment of arterial distension and wall shear rate," *Med. Phys.*, vol. 37, no. 8, pp. 4318–4330, Aug. 2010.
- [22] A. Swillens, G. de Santis, J. Degroote, L. Lovstakken, J. Vierendeels, and P. Segers, "Accuracy of carotid strain estimates from ultrasonic wall tracking: A study based on multiphysics simulations and in vivo data," *IEEE Trans. Med. Imag.*, vol. 31, no. 1, pp. 131–139, Jan. 2012.
- [23] J. Dineley, S. Meagher, T. L. Poepping, W. N. McDicken, and P. R. Hoskins, "Design and characterisation of a wall motion phantom," *Ultrasound Med. Biol.*, vol. 32, no. 9, pp. 1349–1357, Sep. 2006.
- [24] D. N. Ku, "Blood flow in arteries," *Annu. Rev. Fluid Mech.*, vol. 29, pp. 399–434, Jan. 1997.
- [25] T. L. Poepping, N. Nikolov, N. Rankin, M. Lee, and D. W. Holdsworth, "An in vitro system for Doppler ultrasound flow studies in the stenosed carotid artery bifurcation," *Ultrasound Med. Biol.*, vol. 28, no. 4, pp. 495–506, Apr. 2002.
- [26] E. Y. Wong, M. L. Thorne, H. N. Nikolov, T. L. Poepping, and D. W. Holdsworth, "Doppler ultrasound compatible plastic material for use in rigid flow models," *Ultrasound Med. Biol.*, vol. 34, no. 11, pp. 1846–1856, Nov. 2008.

- [27] D. M. King, M. Ring, C. M. Moran, and J. E. Browne, "Development of a range of anatomically realistic renal artery flow phantoms," *Ultrasound Med. Biol.*, vol. 36, no. 7, pp. 1135–1144, Jul. 2010.
- [28] S. Meagher, T. L. Poepping, K. V. Ramnarine, R. A. Black, and P. R. Hoskins, "Anatomical flow phantoms of the nonplanar carotid bifurcation, part II: Experimental validation with Doppler ultrasound," *Ultrasound Med. Biol.*, vol. 33, no. 2, pp. 303–310, Feb. 2007.
- [29] E. Y. Wong, H. N. Nikolov, M. L. Thorne, T. L. Poepping, R. N. Rankin, and D. W. Holdsworth, "Clinical Doppler ultrasound for the assessment of plaque ulceration in the stenosed carotid bifurcation by detection of distal turbulence intensity: A matched model study," *Eur. Radiol.*, vol. 19, no. 11, pp. 2739–2749, Nov. 2009.
- [30] B. Y. S. Yiu and A. C. H. Yu, "High-frame-rate ultrasound color-encoded speckle imaging of complex flow dynamics," *Ultrasound Med. Biol.*, vol. 39, no. 6, pp. 1015–1025, Jun. 2013.
- [31] T. L. Poepping, H. N. Nikolov, M. L. Thorne, and D. W. Holdsworth, "A thin-walled carotid vessel phantom for Doppler ultrasound flow studies," *Ultrasound Med. Biol.*, vol. 30, no. 8, pp. 1067–1078, Aug. 2004.
- [32] S. S. M. Lai, B. Y. S. Yiu, A. K. K. Poon, and A. C. H. Yu, "Design of anthropomorphic flow phantoms based on rapid prototyping of compliant vessel geometries," *Ultrasound Med. Biol.*, vol. 39, no. 9, pp. 1654–1664, Sep. 2013.
- [33] T. L. Poepping, R. N. Rankin, and D. W. Holdsworth, "Flow patterns in carotid bifurcation models using pulsed Doppler ultrasound: Effect of concentric vs. eccentric stenosis on turbulence and recirculation," *Ultrasound Med. Biol.*, vol. 36, no. 7, pp. 1125–1134, Jul. 2010.
- [34] S. Kefayati, D. W. Holdsworth, and T. L. Poepping, "Turbulence intensity measurements using particle image velocimetry in diseased carotid artery models: Effect of stenosis severity, plaque eccentricity, and ulceration," *J. Biomech.*, vol. 47, no. 1, pp. 253–263, Jan. 2014.
- [35] A. C. O. Tsang, S. S. M. Lai, W. C. Chung, A. Y. S. Tang, G. K. K. Leung, A. K. K. Poon, A. C. H. Yu, and K. W. Chow, "Blood flow in intracranial aneurysms treated with pipeline embolization devices: Computational simulation and verification with Doppler ultrasonography on phantom models," *Ultrasonography*, vol. 34, no. 1, pp. 98–108, Jan. 2015.
- [36] C. H. Leow, E. Bazigou, R. J. Eckersley, A. C. H. Yu, P. D. Weinberg, and M.-X. Tang, "Flow velocity mapping using contrast enhanced high-frame-rate plane wave ultrasound and image tracking: Methods and initial *in vitro* and *in vivo* evaluation," *Ultrasound Med. Biol.*, vol. 41, no. 11, pp. 2913–2925, Nov. 2015.
- [37] K. J. M. Surry, H. J. B. Austin, A. Fenster, and T. M. Peters, "Poly(vinyl alcohol) cryogel phantoms for use in ultrasound and MR imaging," *Phys. Med. Biol.*, vol. 49, no. 24, pp. 5529–5546, Dec. 2004.
- [38] P. M. O'Flynn, E. T. Roche, and A. S. Pandit, "Generating an *ex vivo* vascular model," *Amer. Soc. Artif. Internal Organs J.*, vol. 51, no. 4, pp. 426–433, Jul. 2005.
- [39] D. M. King, C. M. Moran, J. D. McNamara, A. J. Fagan, and J. E. Browne, "Development of a vessel-mimicking material for use in anatomically realistic Doppler flow phantoms," *Ultrasound Med. Biol.*, vol. 37, no. 5, pp. 813–826, May 2011.
- [40] T. Khamdaeng, J. Luo, J. Vappou, P. Terdtoon, and E. E. Konofagou, "Arterial stiffness identification of the human carotid artery using the stress-strain relationship *in vivo*," *Ultrasonics*, vol. 52, no. 3, pp. 402–411, Mar. 2012.
- [41] M. Tanter and M. Fink, "Ultrafast imaging in biomedical ultrasound," *IEEE Trans. Ultrason., Ferroelectr., Freq. Control*, vol. 61, no. 1, pp. 102–119, Jan. 2014.
- [42] A. D. Lantada and P. L. Morgado, "Rapid prototyping for biomedical engineering: Current capabilities and challenges," *Annu. Rev. Biomed. Eng.*, vol. 14, pp. 73–96, Aug. 2012.
- [43] R. F. Smith, B. K. Rutt, and D. W. Holdsworth, "Anthropomorphic carotid bifurcation phantom for MRI applications," *J. Magn. Reson. Imag.*, vol. 10, no. 4, pp. 533–544, Oct. 1999.
- [44] J. Krejza, M. Arkuszewski, S. E. Kasner, J. Weigele, A. Ustymowicz, R. W. Hurst, B. L. Cucchiara, and S. R. Messe, "Carotid artery diameter in men and women and the relation to body and neck size," *Stroke*, vol. 37, no. 4, pp. 1103–1105, Apr. 2006.
- [45] R. F. Smith, B. K. Rutt, A. J. Fox, and R. N. Rankin, "Geometric characterization of stenosed human carotid arteries," *Acad. Radiol.*, vol. 3, no. 11, pp. 898–911, Nov. 1996.
- [46] P. R. Hoskins, "Physical properties of tissues relevant to arterial ultrasound imaging and blood velocity measurement," *Ultrasound Med. Biol.*, vol. 33, no. 10, pp. 1527–1539, Oct. 2007.
- [47] K. Zell, J. I. Sperl, M. W. Vogel, R. Niessner, and C. Haisch, "Acoustical properties of selected tissue phantom materials for ultrasound imaging," *Phys. Med. Biol.*, vol. 52, no. 20, pp. N475–N484, Oct. 2007.
- [48] K. V. Ramnarine, D. K. Nassiri, P. R. Hoskins, and J. Lubbers, "Validation of a new blood-mimicking fluid for use in Doppler flow test objects," *Ultrasound Med. Biol.*, vol. 24, no. 3, pp. 451–459, Mar. 1998.
- [49] C. C. P. Cheung, A. C. H. Yu, N. Salimi, B. Y. S. Yiu, I. K. H. Tsang, B. Kerby, R. Z. Azar, and K. Dickie, "Multi-channel pre-beamformed data acquisition system for research on advanced ultrasound imaging methods," *IEEE Trans. Ultrason., Ferroelectr., Freq. Control*, vol. 59, no. 2, pp. 243–253, Feb. 2012.
- [50] H. K. H. So, J. Chen, B. Y. S. Yiu, and A. C. H. Yu, "Medical ultrasound imaging: To GPU or not to GPU?" *IEEE Micro*, vol. 31, no. 5, pp. 54–65, Sep./Oct. 2011.
- [51] B. Y. S. Yiu, I. K. H. Tsang, and A. C. H. Yu, "GPU-based beamformer: Fast realization of plane wave compounding and synthetic aperture imaging," *IEEE Trans. Ultrason., Ferroelectr., Freq. Control*, vol. 58, no. 8, pp. 1698–1705, Aug. 2011.
- [52] D. H. Evans, "Colour flow and motion imaging," *Proc. Inst. Mech. Eng. H, J. Eng. Med.*, vol. 224, no. 2, pp. 241–253, 2010.
- [53] H. Hasegawa, K. Hongo, and H. Kanai, "Measurement of regional pulse wave velocity using very high frame rate ultrasound," *J. Med. Ultrason.*, vol. 40, no. 2, pp. 91–98, Apr. 2013.
- [54] Y. C. Fung, *Biomechanics: Circulation*. 2nd ed. New York, NY, USA: Springer-Verlag, 1997, p. 144.
- [55] E. L. Madsen, M. A. Hobson, H. Shi, T. Varghese, and G. R. Frank, "Tissue-mimicking agar/gelatin materials for use in heterogeneous elastography phantoms," *Phys. Med. Biol.*, vol. 50, no. 23, pp. 5597–5618, Dec. 2005.
- [56] F. Duboef, A. Basarab, H. Liebgott, E. Brusseau, P. Delachartre, and D. Vray, "Investigation of PVA cryogel Young's modulus stability with time, controlled by a simple reliable technique," *Med. Phys.*, vol. 36, no. 2, pp. 656–661, Feb. 2009.
- [57] M. M. Burlew, E. L. Madsen, J. A. Zagzebski, R. A. Banjavic, and S. W. Sum, "A new ultrasound tissue-equivalent material," *Radiology*, vol. 134, no. 2, pp. 517–520, Feb. 1980.
- [58] N. Westerhof and B. E. Westerhof, "Wave transmission and reflection of waves 'The myth is in their use,'" *Artery Res.*, vol. 6, no. 1, pp. 1–6, Jan. 2012.
- [59] C. Huang, T.-L. Ren, and J. Luo, "Effects of parameters on the accuracy and precision of ultrasound-based local pulse wave velocity measurement: A simulation study," *IEEE Trans. Ultrason., Ferroelectr., Freq. Control*, vol. 61, no. 12, pp. 2001–2018, Dec. 2014.
- [60] E. C. Qin, R. Sinkus, G. Geng, S. Cheng, M. Green, C. D. Rae, and L. E. Bilston, "Combining MR elastography and diffusion tensor imaging for the assessment of anisotropic mechanical properties: A phantom study," *J. Magn. Reson. Imag.*, vol. 37, no. 1, pp. 217–226, Jan. 2012.



Adrian J. Y. Chee (S'09) was born in Malaysia. He received the B.Eng. degree (Hons.) in electrical and computer systems engineering from Monash University, Melbourne, VIC, Australia, in 2011. He is currently pursuing the Ph.D. degree with the Biomedical Ultrasound Laboratory, University of Hong Kong. He was a Research Intern with the Hitachi Central Research Laboratory, Tokyo, Japan. His current research interests include the design of new ultrasound-based vascular diagnostic techniques and related experimental tools.



Chung Kit Ho received the B.Eng. degree (Hons.) from the Medical Engineering Program with the University of Hong Kong in 2014. After a brief industry work experience, he returned to the University of Hong Kong in 2015 to work as a Research Engineer in the Biomedical Ultrasound Laboratory. His current research interests include designing novel vascular phantoms for ultrasound imaging investigations.



Billy Y. S. Yiu (M'10) was born in Hong Kong. He is currently a Research Scientist with the Biomedical Ultrasound Laboratory, University of Hong Kong. He received the B.Eng. degree (Hons.) in medical engineering and the M.Phil. degree in electrical and electronic engineering from the University of Hong Kong, in 2007 and 2010, respectively. His current research interests include advanced ultrasound imaging, specifically in the design of high-frame-rate imaging techniques and related system tools. Mr. Yiu was a recipient of the Young Scientist Award at the

2013 Symposium on Ultrasonic Electronics and the Young Investigator Gold Prize Award at the 2014 KSUM Annual Convention.



Alfred C. H. Yu (S'99–M'07–SM'12) is currently an Associate Professor with the Department of Electrical and Computer Engineering, University of Waterloo, ON, Canada. He has a long-standing research interest in ultrasound imaging innovations and therapeutic ultrasound discoveries. He received the bachelor's degree in electrical engineering from the University of Calgary, AB, Canada, in 2002, and the M.A.Sc. and Ph.D. degrees in biomedical engineering from the University of Toronto, ON, Canada, in 2004 and 2007, respectively. He was an

Intern with Philips Research North America, Briarcliff Manor, NY, USA, in 2005. Before he relocated to Waterloo, he was a Research Assistant Professor at the University of Hong Kong, where he founded and served as the Principal Investigator of HKU Biomedical Ultrasound Laboratory. Prof. Yu is a Senior Member of IEEE and AIUM. He is an Associate Editor of the IEEE TRANSACTIONS ON ULTRASONICS, FERROELECTRICS, AND FREQUENCY CONTROL and an Editorial Board Member of ULTRASOUND IN MEDICINE AND BIOLOGY. He also serves on the Technical Program Committee of *IEEE Ultrasonics Symposium* and *International Symposium for Therapeutic Ultrasound*.